We are IntechOpen, the world's leading publisher of Open Access books Built by scientists, for scientists

4,800
Open access books available

122,000
International authors and editors

135M
Downloads

Our authors are among the

154
Countries delivered to

TOP 1%
most cited scientists

12.2%
Contributors from top 500 universities

WEB OF SCIENCE™

Selection of our books indexed in the Book Citation Index in Web of Science™ Core Collection (BKCI)

Interested in publishing with us?
Contact book.department@intechopen.com

Numbers displayed above are based on latest data collected.
For more information visit www.intechopen.com

9

Fe-Based Nanocomposite Formed by Thermal Treatment of Rapid-Quenched $Fe_{81}B_{13}Si_4C_2$ Alloy

Dragica M. Minić[1], Vladimir A. Blagojević[1] and Dušan M. Minić[2]
[1]*University of Belgrade, Faculty for Physical Chemistry,*
[2]*Military Technical Institute, Belgrade,*
Serbia

1. Introduction

Amorphous alloys have been a focus of considerable scientific interest, both from fundamental and practical point of view, ever since the first of its kind ($Al_{75}Si_{25}$) was produced by Klement, Willens and Duwez in 1960 (Klement et al., 1960). It has been shown that the amorphous alloys have features that are different from those of crystalline alloys in both alloy compositions and atomic configurations. This enabled the exhibition of various characteristics which were not obtained for conventional crystalline alloys. Their soft ferromagnetic properties (saturation magnetization, high permeability, low coercivity and loss), high corrosion resistance and good mechanical properties make them suitable for use in a variety of applications, such as power devices, information handling technology, magnetic sensors, anti-theft security systems and construction materials (Minić et al., 2007). Since amorphous alloys are meta-stable, elevated temperature or prolonged performance can induce a transformation into a crystalline state, which could lead to a loss of their advantageous physical properties limiting them to single-use applications. Commercial soft magnetic nanocrystalline materials have recently been successfully obtained by crystallization of amorphous precursors. Materials like this are characterized by a microstructure of nanocrystals embedded into an amorphous matrix, exhibiting superior soft magnetic and mechanical properties to both amorphous and crystalline magnetic alloys (Blagojević et al., 2011; Minić et al., 2011a). This dependence of functional properties on microstructure can be used to produce functional materials with tailored properties (Maričić et al., 2012).

The production of early amorphous alloys required very high cooling rates (as much as 10^6 K/s) to avoid crystallization. This limited the form in which they could be produced, as one dimension had to remain small enough to allow sufficiently rapid heat extraction, in order to achieve the necessary high cooling rates. The result was that the thickness of amorphous metal specimens was limited to less than 100μm. In 1976, Liebermann and Graham developed a new method of manufacturing thin ribbons of amorphous metals on a supercooled rapidly rotating disc – the melt-spinning method (Liebermann & Graham, 1976). For the next thirty years, with the production of new materials, the required cooling rate diminished, until, in 1990s, materials were developed, whose production required cooling rates as low as 1 K/s, allowing these alloys to be cast into metallic moulds to

produce specimens up to 100mm thick (Ponnambalam et al., 2004). The alloys that require cooling rates below 10^3 K/s are known as bulk amorphous alloys, as the production process allows for higher specimen thickness (above 1mm), classifying them as bulk materials.

2. Experimental procedures

The ribbon shaped samples of $Fe_{81}B_{13}Si_4C_2$ amorphous alloy were obtained using the standard procedure of rapid quenching of the melt on a rotating disc (melt-spinning method). The obtained ribbon was 2 cm wide and 35 μm thick. During the preparation process of the amorphous alloy ribbon, one of the sides was in direct contact with the cooled rotating disc, while the other was in inert atmosphere. As a result, the two sides of the ribbon show an easily observable difference in reflectivity, surface morphology and structure, as can be seen in X-ray diffraction (XRD) spectra, Fig.1, as well as SEM images of the sample in the as-prepared alloy (Fig.2). The side that was in the contact with the cooled spinning disc is usually labeled as fishy or matte side and the other side, free of contact, as shiny side.

DSC was obtained using SHIMADZU DSC-50 analyzer. In this case, samples weighting several milligrams were heated in the DSC cell from the room temperature to 650°C in a stream of nitrogen with nitrogen flowing at a rate of 20 mL min^{-1} at the heating rates of 5, 10, 20 and 30°Cmin^{-1}.

Mössbauer spectra were taken in the standard transmission geometry using a ^{57}Co(Rh) source at room temperature. The calibration was done against α-Fe foil data. "CONFIT" program package was used for the spectra fitting and decomposition (T. Žák, 1999).

The X-ray diffraction (XRD) patterns were recorded on an X'Pert PROMPD diffractometer from PANalytical with CoKα radiation operated at 40kVand 30mA. For routine characterization, diffraction data was collected in the range of 2θ Bragg angles (15–135°, step 0.0081). For a quantitative analysis and determination of crystallite size from XRD spectra, TOPAS V3 general profile and structure analysis software for powder diffraction data was used (BrukerAXS, general profile and structure analysis software for powder diffraction data, Karlsruhe, 2005). Dislocation density was obtained from the Rietveld analysis, while microstrain was calculated using Williamson-Hall method (Williamson, Hall 1953), using the XRD data. Lattice parameters obtained through XRD spectra were used to calculate the unit cell volumes, which were then compared to the standard values in JCPDS database.

Vickers microhardness tests were performed using MHT-10 (Anton Paar, Austria) microhardness tester, with loads of 0.4N and loading time of 10s (Minić, et al. 2011c). Up to seven measurements were performed on each individual sample, using the average value of microhardness for each sample. The measurements were performed on the cross-section of the ribbons, rather than on any of the sides. Error was calculated as standard deviation for each series of measurements.

2.1 Microstructure of as-prepared $Fe_{81}B_{13}Si_4C_2$ amorphous alloy

XRD spectra of the as-prepared alloy ribbon, Fig.1, showed that the as-prepared alloy already had a degree of crystallinity caused by presence of α-Fe phase (JCPDS-PDF 06-0696). The degree of crystallinity is much higher on the shiny side, with peak intensity in XRD spectrum being about 8 times higher on the shiny side.

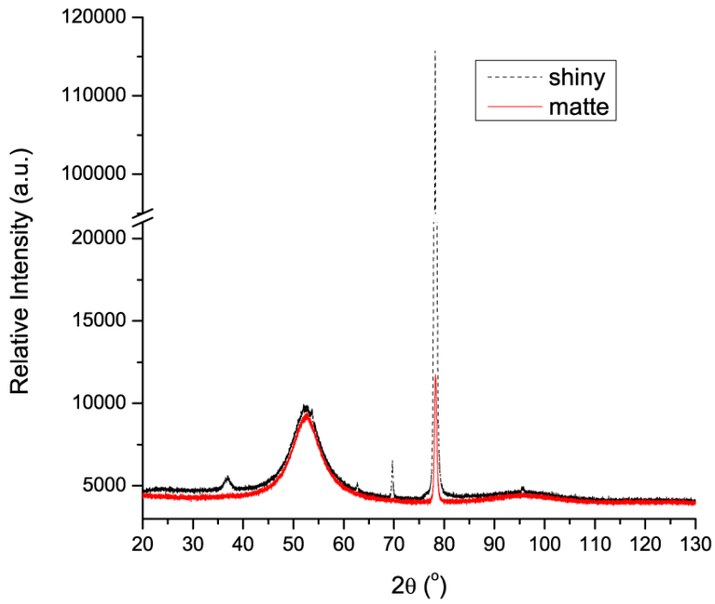

Fig. 1. X-ray diffraction spectra of as-prepared alloy

The nanocrystalline phase can be identified as α-Fe on matte side and a mixture of α-Fe and Fe_3Si on shiny side, with α-Fe being the major component. In addition to sharp crystalline peaks (37, 69 and 78°) in the XRD spectra of the as-prepared alloy, a broad spread halo around 53°, corresponding to domains of short-range ordering in the sample, was also observed. The position of the spread halo corresponds to approximate position of Fe_3Si peak and, using the Scherrer equation, we estimated the size of these domains to be 1-1.5 nm. The entire structure could best be described as a combination of nanocrystals and short-range ordered domains embedded in an amorphous matrix. Recent theoretical studies of iron-based binary systems predict existence of short-range ordering in iron-based amorphous alloys (Lass et al., 2010). Therefore, appearance of domains of short-range ordering in $Fe_{81}B_{13}Si_4C_2$ amorphous alloy could be expected.

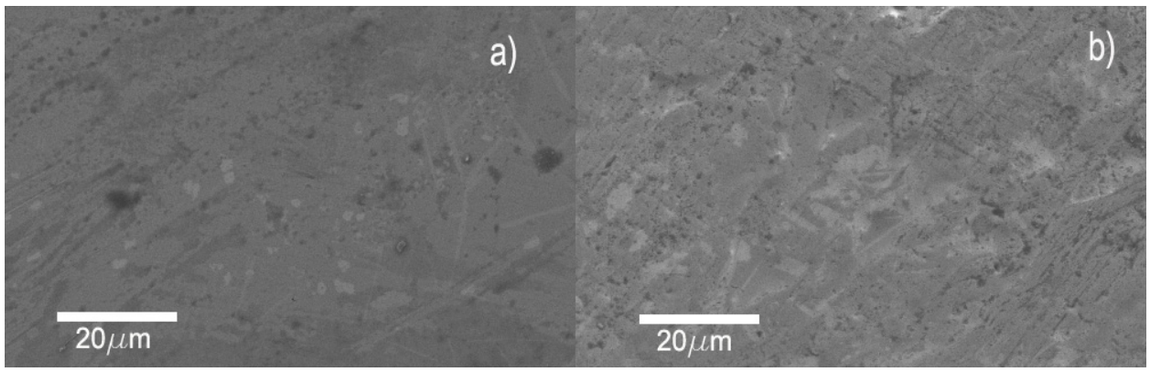

Fig. 2. SEM of as-prepared $Fe_{81}B_{13}Si_4C_2$ amorphous alloy (a – shiny; b – matte side)

Crystal structures of α-Fe and Fe_3Si are closely related, as Fe_3Si crystal system is cubic, same as α-Fe crystal system. Fe_3Si lattice is composed of four sub-lattices: three composed of iron atoms and one of silicon atoms, and this leads to doubling of the unit cell (when compared

to α-Fe). Fe_3Si lattice is, also, slightly distorted, so the value of its lattice parameter is slightly higher than twice the value of lattice parameter of α-Fe.

2.2 Thermal stability of alloy

The thermal stability of the alloy was investigated using differential scanning calorimetry (DSC) in a nitrogen atmosphere (Minić, et al., 2009a). Typical DSC scan obtained during heating and cooling cycle is presented in Fig. 3. DSC scan involves a series of endothermic and exothermic peaks indicating a stepwise process of structural stabilization of the alloy in the temperature range 170-560°C. A broad exothermic peak, indicated as (T_{sr}), in temperature range 170-400°C, coresponding to structural relaxation, is followed by endothermic hump (temperature of glass transition T_g) and a short supercooled liquid region before the sharp exothermic crystallization peak (T_k) in temperature range 500-540°C. The enthalpy of crystallization is 83.5 J/g as determined from area of corresponding peak obtained at heating rate of 20 °Cmin^{-1}.

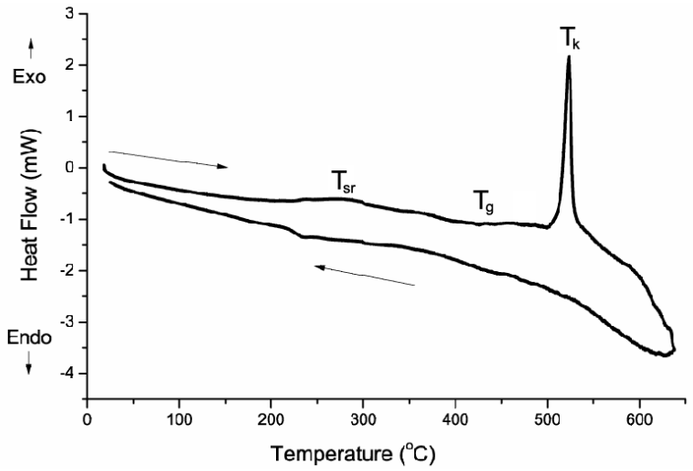

Fig. 3. DSC scan of heating and cooling cycle in nitrogen atmosphere; heating rate 10°C/min.

2.3 Magnetic properties

2.3.1 Thermo-magnetic behavior

Thermally induced processes were also studied using the thermo-magnetic scan, where the sample is heated, annealed and then cooled in vacuum furnace at low magnetic field of 4 kA·m^{-1} while its magnetic moment is monitored (Minić, et al., 2011b). Both heating and cooling rate were 4°C·min^{-1}, dwell time at maximum temperature of 800°C was 30 minutes. The shape of the thermo-magnetic curve, Fig. 4, reflects changes in the magnetic moment of the sample, caused by phase or structural transitions.

Most pronounced change represents the Curie point (T_c = 420°C), where the magnetization of the respective phase drops to almost zero, because the thermal motion overcomes magnetic interaction. Annealing at the temperature near 200°C is sometimes called stress-relieving (or structural relaxation). Temperatures marked by arrows in Fig. 4 have been identified as points of interest for further study of structural transformations.

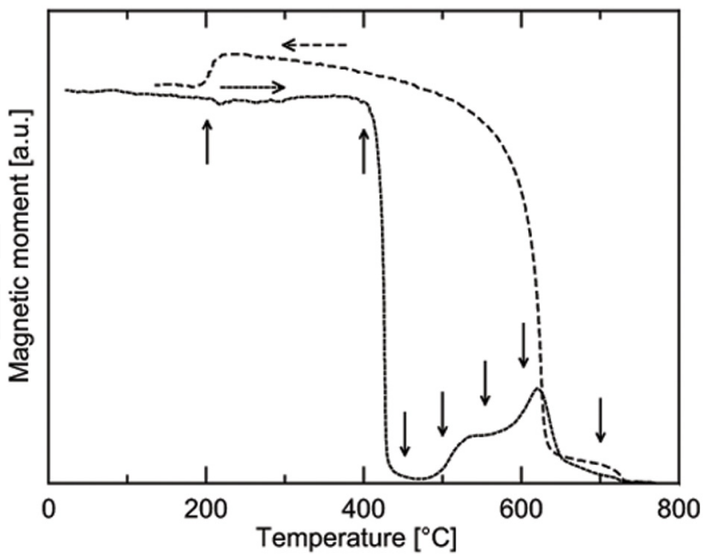

Fig. 4. Thermomagnetic scans for increasing (dotted line) and decreasing (dashed line) temperature.

2.3.2 Magnetic susceptibility

Measurements of relative magnetic susceptibility were performed using a modified Maxwell method, based on the action of an inhomogeneous field on the magnetic sample. The magnetic force measurements were performed with a sensitivity of 10^{-6}N in an argon atmosphere (Minić, et al. 2009b).

The temperature dependence of the relative magnetic susceptibility of the as-prepared $Fe_{81}B_{13}Si_4C_2$ amorphous alloy during three thermal treatments to different temperatures is presented in Fig. 5. During the first and second treatment, the decrease in the magnetic susceptibility in the temperature region from 320°C to 380°C is the result of proximity to the Curie temperature of the amorphous alloy. Before the start of the second treatment it was observed that magnetic susceptibility increased slightly. This was caused by the structural relaxation of an amorphous structure during the first treatment. During this process, internal strains and the free volume are reduced in the starting material. These changes are accompanied by subtle inter-atomic movements, causing the changes in the electron structure and leading to an increase in the number of electrons with unpaired spin in the direction of the outer magnetic field (Minić et al., 2009b). This also leads to a decrease in the number of electrons spinning in the reverse direction and causes an increase in the magnetic susceptibility upon cooling. At the same time, strains and decrease in the free volume enable greater mobility of the walls of the magnetic domains and this behavior further contributes to the increase in the magnetic susceptibility.

During the second treatment, the alloy loses its ferromagnetic properties in the temperature region from 400°C to 470°C. With further heating, the magnetic susceptibility starts to rise, and the alloy regains its ferromagnetic properties once the crystallization process starts at about 490°C. After the second heating to 490°C, the magnetic susceptibility decreases by 23 % when compared to the value of as-prepared alloy and to the value of the relaxed state of

the lattice after the first heating cycle. During the third treatment, above the crystallization temperature, the alloy maintains its ferromagnetic features in the whole temperature region, whereas the maximum change in the magnetic susceptibility occurs at about 190°C as a consequence of further phase transformation of the crystallized alloy.

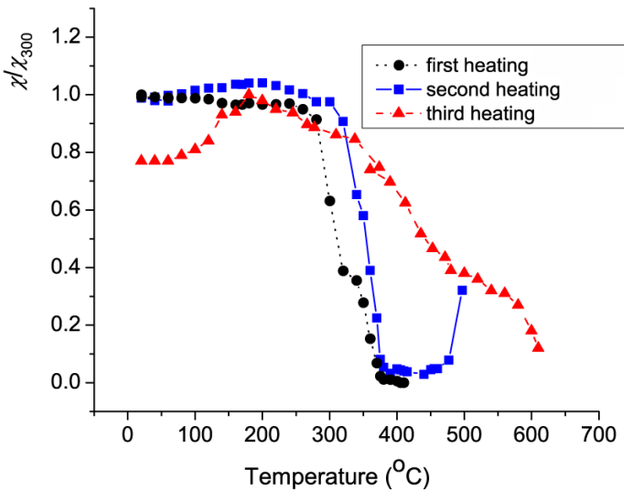

Fig. 5. Temperature dependence of relative magnetic susceptibility of as-prepared $Fe_{81}B_{13}Si_4C_2$ amorphous alloy during three thermal treatments up to different temperatures: a) 420°C; b) 500°C; c) 630°C.

2.3.3 Mössbauer spectra

In the Fig. 6, spectra illustrate the ability of Mössbauer effect to distinguish between individual iron-containing phases of different structure. Broad-line components (Fig. 6a) are

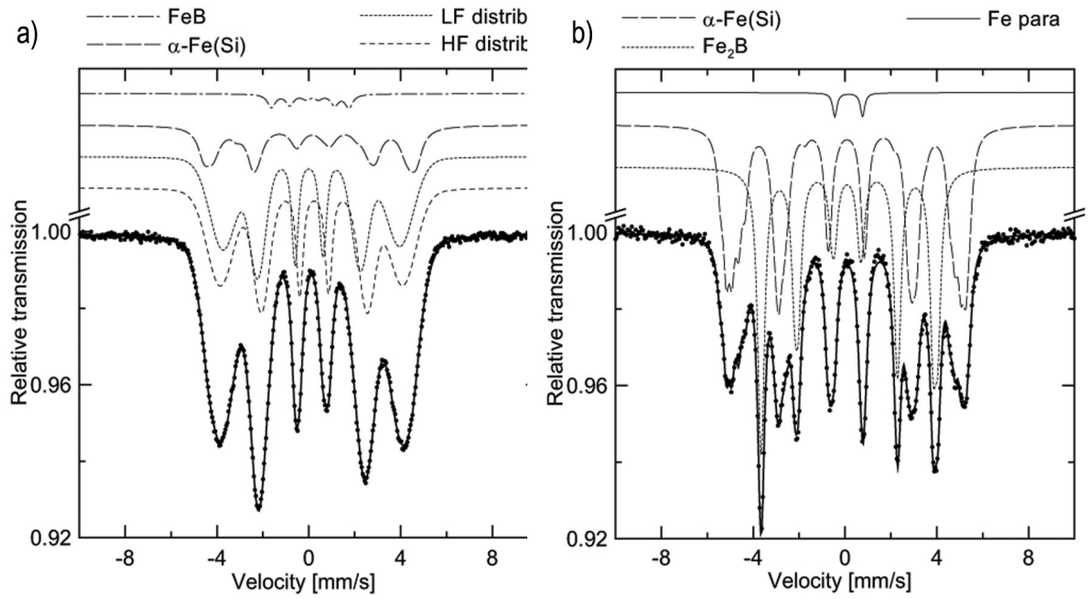

Fig. 6. Mössbauer spectra of the as-prepared material (left) and of material after final annealing at 700°C (right), including components of iron containing phases.

typical for the amorphous volume of the as-prepared sample, while the sharp lines (Fig. 6b) characterize the crystalline structure with well defined position of atoms, which results from the thermally induced crystallization process during annealing of the sample (Minić, et al. 2011b). The computer processing of Mössbauer spectra yielded intensities, I, of components, their hyperfine inductions, B_{hf}, isomer shifts, δ, and quadrupole splitting, σ (T. Žák & Y. Jirásková, 2006). The contents of the iron-containing phases are determined as proportional to the relative areas of the corresponding spectral components. The phase percentages correspond to the distribution of Mössbauer iron atoms among phases (Table 1).

Annealing temperature	Amorphous at%	α-Fe(Si) at%	Fe_2B at%	Fe_3B at%	FeB at%	α-Fe at%	Fe para at%
as-prepared alloy	0.95	0.03	–	–	0.02	–	–
200°C/30 min.	0.94	0.02	–	–	0.02	0.02	–
450°C/30 min.	0.83	0.14	–	0.03	–	–	–
500°C/30 min.	–	0.42	0.42	0.15	–	–	0.01
550 °C/30 min.	–	0.52	0.47	–	–	–	0.01
600°C/30 min.	–	0.54	0.45	–	–	–	0.01
700°C/30 min.	–	0.55	0.44	–	–	–	0.01

Table 1. Mössbauer tentative phase analysis (distribution of Mössbauer iron atoms among phases) (Minić, et al. 2011e)

In the as-prepared alloy, the amorphous structure, having a high-field and a low-field component is accompanied by a small amount of α-Fe(Si) solid solution and a FeB phase. Mössbauer phase analysis at higher temperatures reveals α-Fe(Si) solid solution and Fe_2B phase to be the most important final crystallization products, although metastable phase Fe_3B, was detected initially at 450°C and in higher percentage at 500°C. Amount of iron atoms in paramagnetic positions is almost below the sensitivity threshold. Content of silicon in the α-Fe(Si) solid solution seems to be about 9 at.%, which is close to 7 at.% published in (Saegusa & Morrish, 1982).

2.4 Electrical properties

2.4.1 Electrical resistance

The electrical resistance of the ribbon was measured using the four-point method within a temperature interval of 20–630°C in an argon atmosphere (Minić, et al., 2011d). Fig. 7a shows the temperature dependence of the electrical resistivity of the alloy in the temperature range of 25-630°C. The dependence clearly shows each structural stabilization step which causes the change in the ordering of the investigated material. These changes are more obvious in the derivative curve (Fig. 7b).

The slow increase of electrical resistivity was caused by the structural relaxation process in the temperature range of 200-380°C. This process is followed by an increase of electrical resistivity in the vicinity of Curie temperature T_c at 420°C, corresponding to the first maximum of the differential curve. At this point the effect that scattering of conductive electrons had on the magnons disappeared (I. Balberg & J. S. Helman, 1978; G. Bohnke et al., 1983) and the amorphous alloy loses its ferromagnetic properties (D. M. Minić et al. 2010). This is in excellent agreement with the results of the thermo-magnetic measurements (Fig.

4). The beginning of crystallization at about 520°C caused a sharp decrease of electrical resistivity. The appearance of two clearly separated maxima, T_{k1} and T_{k2} (490 and 510°C respectively) on the differential curve of electrical resistivity (Fig. 7b), suggests that crystallization of the amorphous alloy is a complex process, occurring in two steps, which appear as a single overlapping peak in the DSC scans, Fig. 3.

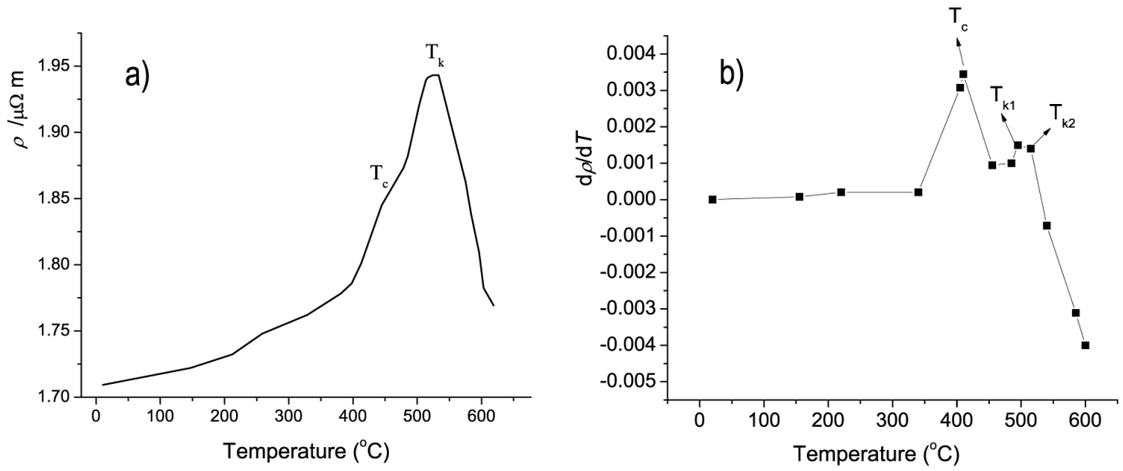

Fig. 7. Temperature dependence of the electrical resistivity of amorphous alloy.

The electrical resistivity of the crystalline alloy is lower than that of the amorphous alloy of the same composition, as a result of the increase in electron free path. The linear change of electrical resistivity with increasing temperature during the second treatment shows that crystallization was completed during the first heating cycle (Fig. 8).

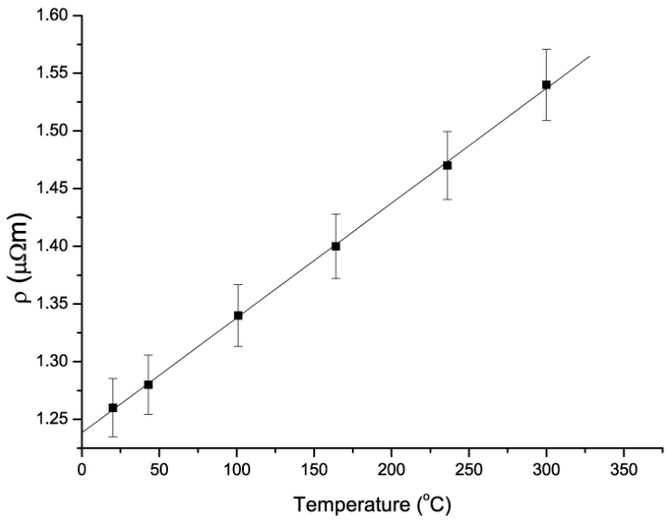

Fig. 8. Temperature dependence of the electrical resistivity of second thermal treatment

2.4.2 Thermo-electromotor force

The structural relaxation processes, as well as the crystallization, in the temperature interval of 25-680°C, were also investigated by measuring the thermo-electromotor force (TEMF) of a

thermocouple made by coupling a copper conductor to the amorphous alloy (D.M. Minić, et al. 2009b). The alloy sample was mechanically attached to a copper conductor, forming the Cu – $Fe_{81}B_{13}Si_4C_2$ thermocouple, which was placed into a specially designed furnace, while the other end of the sample was submerged into a mixture of water and ice. The TEMF produced by the thermocouple during the heating process was measured by a voltmeter with the sensitivity of 10^{-5}V.

The temperature dependence of a thermo-electromotor force (Fig. 9) shows three linear regions corresponding to the structural transformations of the alloy. Different slopes of these linear dependences correspond to structural changes involving a structural relaxation, the loss of ferromagnetic properties, and the crystallization, respectively. The temperature coefficient of TEMF is a function of the electron state density at the Fermi level:

$$\alpha = \frac{k}{2e}\left(\frac{N_{1E_F}}{N_{2E_F}} - \frac{N_{2E_F}}{N_{1E_F}}\right) \tag{1}$$

where k is Boltzmann's constant, e is electron charge, $N_{1(Ef)}$ is the electron state density in copper and $N_{2(Ef)}$ is the electron state density in the alloy.

The electron density of states in copper remained unchanged during heating to 680°C, meaning that the change in the temperature coefficient during the heating of the thermocouple was caused only by the change of the electron density of states at the Fermi level of the alloy. Based on the slope of the first linear segment in Fig. 9, temperature coefficient a_1= 9.4 μV/K, and the relative change in the electron density of states of the alloy caused by the structural relaxation process was determined to be $\frac{\Delta N_1}{N} = 3.53\%$. The temperature coefficient for the second linear segment is a_2= 8.36 μV/K, and $\frac{\Delta N_2}{N} = 5.33\%$

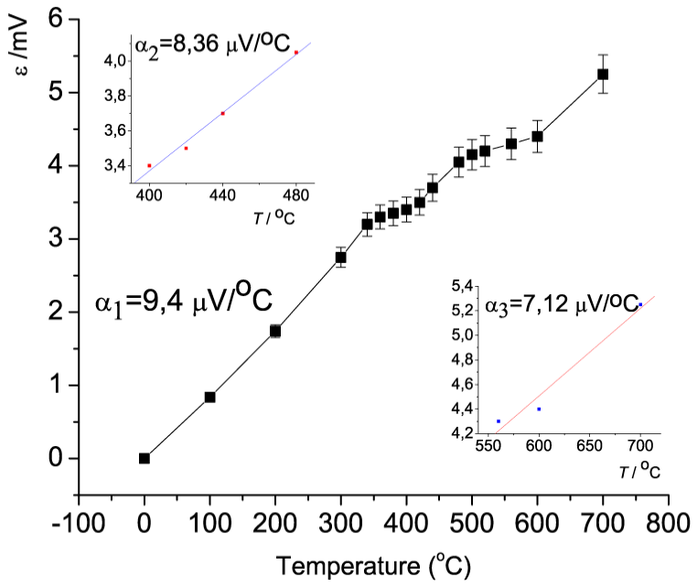

Fig. 9. Temperature dependence of thermo-electromotor force.

was determined to be 5.33% and for the third linear segment a_3= 7.12 μV/K and $\frac{\Delta N_3}{N} = 7.81\%$ was 7.81%. The overall change in the electron density of states at the Fermi level caused by the structural transformations during heating the alloy in temperature range 25-680°C is the sum of the three ΔN/N values and equals 16.67%.

The increase in the electron density of states at the Fermi level and the above mentioned increase in free path of the electron combine to diminish resistivity of the crystalline alloy (Fig. 8).

2.5 Structural transformations induced by thermal treatment

X-ray diffraction (XRD) spectra of the alloy ribbon samples (Fig. 10) show that thermal treatment (200-700°C) caused a series of structural transformations of the amorphous alloy leading to formation of more than one crystalline phase: the stable α-Fe, Fe_3Si and Fe_2B as well as metastable Fe_3B. Crystallization initially leads to formation of a nanocomposite structure of nanocrystals dispersed in the amorphous matrix. After thermal treatment at 700°C, the alloy ribbon sample was fully crystallized and composed of interdispersed nanocrystals of three crystalline phases: α-Fe, Fe_3Si and Fe_2B. The analysis of crystallite orientation on the two sides of the ribbon showed that Fe_3Si and α-Fe crystallites exhibit a degree of preferential orientation after thermal treatment. In the as-prepared alloy, Fe_3Si and α-Fe crystallites on the shiny side are oriented preferentially in [100] direction, while those on the matte side are not. This is probably the reason for higher reflectivity of the shiny side of the ribbon and the consistently high intensity of peak around 78° in the XRD spectra of the shiny side. After the treatment at 500°C, the degree of preferential orientation increases on the shiny side and forms on the matte side, suggesting asymmetric growth of the crystallites. After treatment at 700°C, amplitudes of the degree of preferential orientation on both sides decreased, suggesting that the crystallites were growing in more symmetrical manner. All of these changes are much more pronounced on the shiny side than on the matte side.

Rietveld analysis (Minić, et al. 2011c, Fig. 11) of XRD spectra yielded phase composition of the crystalline portion of the samples, average crystal sizes, dislocation density and microstrain for individual phases (Table 2). R^2 was greater than 0.98 for all XRD measurements. Individual phase contributions of α-Fe and Fe_3Si could not be completely separated, because of the overlap of their peaks. The phase composition data shows that shiny side has higher percentage of metastable Fe_3B phase, but lower percentage of Fe_2B phase. After heating at 700°C, the final phase composition on the matte side shows more crystalline Fe_2B than on the shiny side. The phase content of Fe_3B declines in two steps, with increase in heating temperature, to disappear completely after thermal treatment at 650°C. The first sharp decrease in percentage of Fe_3B (550°C) coincides with an increase in percentage of combined α-Fe and Fe_3Si. After thermal treatment at 650°C, Fe_3B phase disappears completely, and this coincides with increase in phase content of Fe_2B. Phase content of Fe_2B phase shows an increase after treatment at temperatures above 550°C.

The evolution of average crystal sizes for the respective phases shows that while there is some difference between shiny and matte side of the ribbon at the onset of crystallization, those differences become almost negligible after heating at 700°C. On closer examination, Fe_3Si and α-Fe have lower crystal sizes on the matte side, at heating temperatures of 500°C

and below, and then grow faster than they do on the shiny side. As a consequence, crystal sizes of Fe_3Si and α-Fe, respectively, at the end of crystallization are almost the same on both sides of the ribbon. The evolution of average crystal size of Fe_2B shows the same trend of smaller initial crystal size and then faster crystal growth on the matte side, with increase in temperature. Metastable Fe_3B phase shows the same trend with regards to growth, except, it has a higher average crystal size on the matte side, after the samples are treated at 500°C.

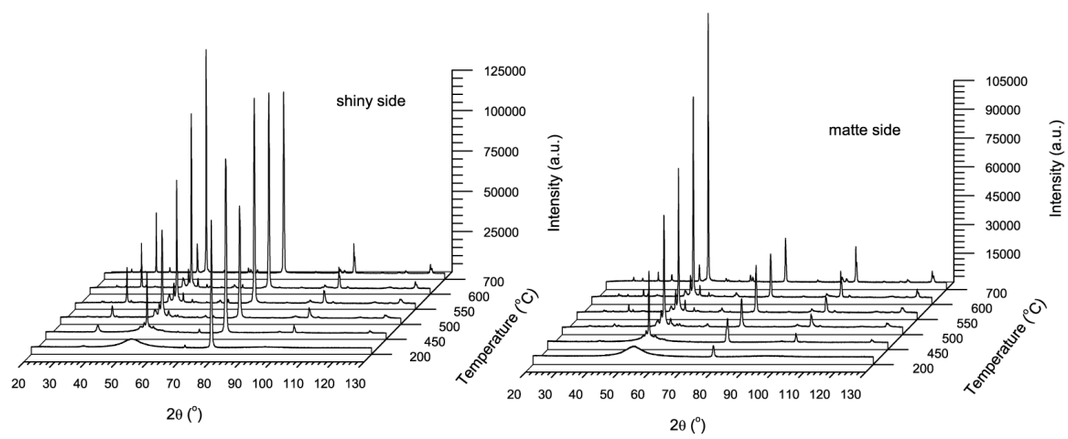

Fig. 10. XRD spectra of alloy samples after thermal treatment (left – shiny side; right – matte side)

In order to further comprehend the changes in phase composition, unit cell volumes for individual phases were determined using XRD data, and compared with standard values in JCPDS database (Minić, et al. 2011c). This way, we estimated the lattice distortion caused by the presence of boron in α-Fe and Fe_3Si lattices. The change in unit cell volume was negative for α-Fe and positive for Fe_3Si phase. The diagram (Fig 12) shows that the distortion of the unit cell of α-Fe was the greatest before the crystallization started; it decreased during the crystallization and remained relatively stable after treatment at 500°C and higher temperatures.

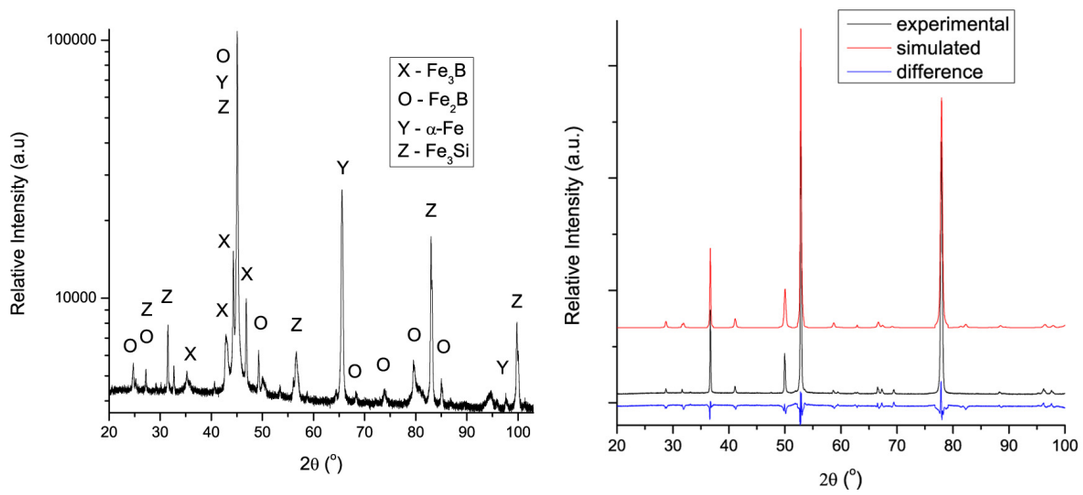

Fig. 11. XRD spectrum of alloy sample treated at 600°C with individual peak assignments (left); Rietveld analysis of XRD spectrum of alloy sample treated at 700°C (right)

The change in Fe_3B percentage after treatment at 550°C was accompanied by a decreased distortion of the unit cell of both α-Fe and Fe_3Si and increase in their combined phase content. This indicates that iron from Fe_3B was transformed into these two phases, with boron being incorporated back into the α-Fe/Fe_3Si matrix. As Fe_3Si showed greater change, Fe_3B probably transformed more to Fe_3Si than it did to α-Fe.

Temperature °C	Matte				Shiny			
	α-Fe	Fe_3Si	Fe_2B	Fe_3B	α-Fe	Fe_3Si	Fe_2B	Fe_3B
Phase composition (% mass of crystalline phase)								
500	84± 4		8± 2	8± 4	83± 5		6± 2	11± 2
550	88± 3		8± 2	4± 1	88± 3		8± 2	4± 1
600	86± 3		10± 2	4± 1	89± 3		8± 2	3± 1
700	87± 2		13± 2	-	90± 2		10± 2	
Average crystal size (nm)								
25	26.2				36.9			
200	24.6				36.5			
450	19.7				32.9			
500	26.7	22.3	49.3	16	33.1	35.1	37.3	15.8
550	32.1	35.4	90.6	46.4	36.4	45.6	82.7	44.8
600	38.6	51.6	97.7	56.6	39.0	52.7	111.1	67.7
700	44.6	71.9	107.5	-	44.9	67.5	133.5	
Dislocation density (10^{15} m^{-2})								
25	4.37				2.2			
200	4.96				2.25			
450	7.73				2.77			
500	4.21	6.03	1.23	11.72	2.74	2.43	2.16	12.02
550	2.91	2.39	0.37	1.39	2.26	1.44	0.44	1.50
600	2.01	1.13	0.31	0.94	1.97	1.08	0.24	0.66
700	1.51	0.58	0.26	-	1.49	0.66	0.17	
Microstrain (%)								
25	2.19				2.47			
200	1.85				2.63			
500	2.53				3.56	4.73		
550	2.00	4.27			2.26	3.76		
600	1.94	4.03			1.70	5.69		
700	1.26	3.47			1.37	2.66		

Table 2. Phase composition and dislocation density in the samples, obtained by analysis of XRD data

Reduced lattice distortion in these phases is probably due to the fact that mass percentage of boron in Fe_3B (6.06%) is lower than the mass percentage of boron in the as-prepared alloy (13%). Therefore, transformation of Fe_3B would lead to dilution of boron in α-Fe/Fe_3Si matrix, leading to stabilization of its crystal structure. The change in unit cell volumes of Fe_3Si and α-Fe showed increase at higher heating temperatures and it is possible that the distortion of the lattice in α-Fe and Fe_3Si is caused by the increasing occurrence of crystal/crystal interfaces between α-Fe and Fe_3Si on one side and Fe_2B on the other.

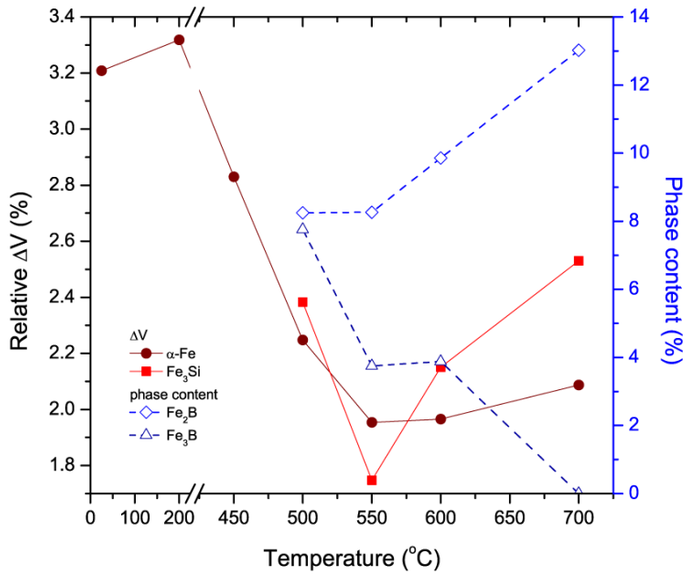

Fig. 12. Change in unit cell volumes of α-Fe and Fe_3Si against change in phase contents of Fe_2B and Fe_3B

2.6 Mechanical properties

Microhardness was measured on the cross-section of the alloy ribbon samples, rather than on any of the sides, giving a good measure of the average properties of the alloy samples. This was done due to extreme brittleness of the ribbon samples after crystallization. In order to clearly show the influence of the change in microstructure, induced by thermal treatment, on microhardness, we presented the microhardness data in combination with DSC scan (Fig. 12). In terms of microstructure, the as-prepared alloy contains a small percentage (less than 5%) of crystalline α-Fe phase in form of nanocrystals dispersed in the amorphous matrix (Fig. 1) and small domains (1-1.5 nm in size) of short-range crystalline ordering. This structure can be best described as a nanocomposite of nanocrystals and nanoclusters embedded in the amorphous matrix. The nanocomposite structure combines with chemical composition, involving significant percentage of boron, silicon and carbon, all of which are known to increase hardness in iron alloys, to produce high hardness of the as-prepared alloy sample (909HV).

The change of microhardness with respect to heating temperature showed three distinct temperature regions with completely different behavior. Before the onset of crystallization around 450°C, microhardness exhibited slight growth, from 909 to 931HV, which corresponds to lattice relaxation, as shown by the broad exothermic peaks in 200-400°C region in the DSC (Fig. 13a). In the second region, after thermal treatment at 450°C, it increased to 951HV and then to 1250HV, after thermal treatment at 500°C. This corresponds to crystallization involving formation of disordered Fe_3Si crystal phase (around 450°C), stable crystalline phases Fe_3Si, Fe_2B, α-Fe and metastable Fe_3B (exothermic peak around 512°C). These phases form a nanocomposite of nanocrystals dispersed in the amorphous matrix, which is the main cause of the increased microhardness. In the last temperature region, after the sample was treated at 700°C, microhardness decreased to 908HV, as a consequence of further crystal growth, leading to the change in the nature of the interfaces.

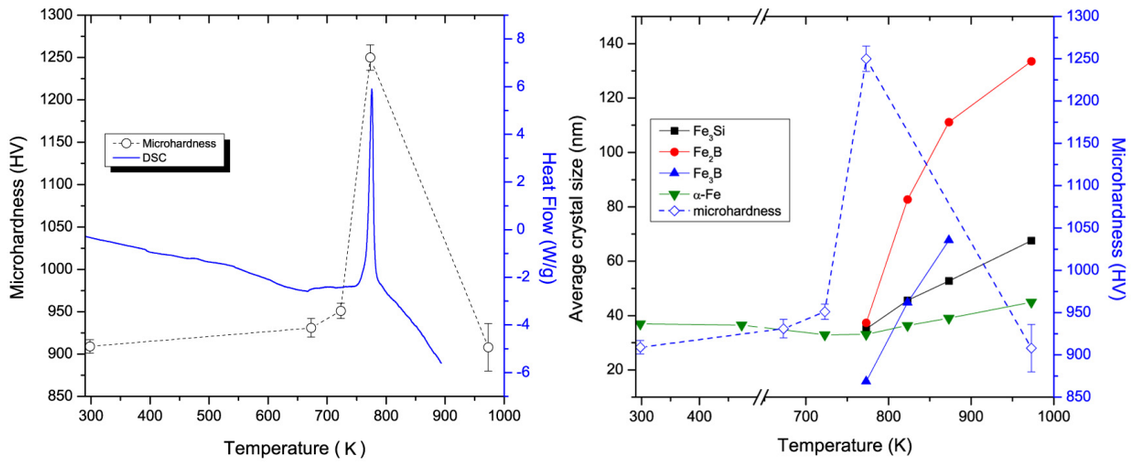

Fig. 13. Microhardness shown with DSC scan (a) and average crystal size on matte side (b).

These changes in microhardness can also be correlated with change in microstructure, induced by thermal treatment, through evolution of average crystal size of the crystalline phases in the alloy (Fig. 13b) (Minić, et al. 2011c). It can be seen that average crystal size has a significant influence on the change in microhardness. When the formed nanocrystals are relatively small (below 50 nm), microhardness remains high, while appearance of larger nanocrystals (over 100 nm) leads to a sharp decrease in microhardness. After thermal treatment at temperatures from 200 to 700°C, the alloy structure gradually transformed from a relatively homogeneous to a granulated structure with larger crystalline domains. This is consistent with creation, at the beginning of the crystallization, of a nanocomposite of small nanocrystals dispersed in amorphous matrix, which significantly increases microhardness, due to the fact that the dominant type of interface in the alloy is crystal/amorphous, as opposed to crystal/crystal in a completely crystalline alloy. As the average crystal size increased, crystal/crystal interfaces became dominant and microhardness decreased, due to increased interfacial energy and more successful propagation of shear bands and cracks along these interfaces. During the course of the observed structural transformations, the overall composition of the alloy did not change drastically, while microhardness showed significant fluctuation. This means that the changes of microhardness in our alloy were caused primarily by changes in its microstructure, rather than changes in its composition, with the main factor being the change in the average crystal size and creation of a granulated structure, as opposed to nanocrystals embedded in amorphous matrix (Table 2). The granulated structure, in addition to containing larger crystals and more crystal/crystal interfaces, is also much more porous than the original nanocomposite crystal/amorphous structure of the as-prepared alloy.

2.7 Kinetics of crystallization

All kinetic studies assume that the isothermal rate of conversion dα/dt is a linear function of the temperature-dependent reaction rate constant, k (T), and a temperature-independent function of the conversion, f (α) (Vyazovkin, 2000)

$$\frac{d\alpha}{dt} = k(T) f(\alpha), \tag{2}$$

where a is the fractional extent of reaction (conversion degree), t is time and the function $f(\alpha)$ depends on the particular crystallization mechanism.

The temperature dependence of the rate conversion is introduced by replacing $k(T)$ with the Arrhenius equation, which gives the relation

$$\frac{\mathrm{d}\alpha}{\mathrm{d}t} = A\exp\left(-\frac{E}{RT}\right)f(\alpha) \tag{3}$$

where A (pre-exponential factor) and E (activation energy) are the Arrhenius parameters and R is the gas constant.

Kinetic description of solid state transformations usually includes a kinetic triplet, involving Arrhenius parameters (activation energy, E and pre-exponential factor, A) as well as an algebraic expression of the conversion function, $f(a)$ (presented in Table 3), which describes the dependence of the reaction rate on the conversion degree, a.

In solid state reactions, the constant value of activation energy can be expected only for a single-step reaction, therefore E in equation (3) becomes an apparent quantity (E_a), based on a quasi-single-step reaction. In non-isothermal measurements at constant heating rate, β, the equation (3) transforms to:

$$\beta\frac{\mathrm{d}\alpha}{\mathrm{d}T} = A\exp\left(-\frac{E_a}{RT}\right)f(\alpha) \tag{4}$$

where $\mathrm{d}\alpha/\mathrm{d}t \equiv \beta\,(\mathrm{d}\alpha/\mathrm{d}T)$.

The integral form of the reaction model can be obtained by integration of equation (4)

$$g(\alpha) = \int_0^{\alpha}\frac{\mathrm{d}\alpha}{f(\alpha)} = \frac{AE_a}{R\beta}p(x) \tag{5}$$

where $p(x)$ is the temperature integral for $x=E_a/RT$ which does not have analytical solution.

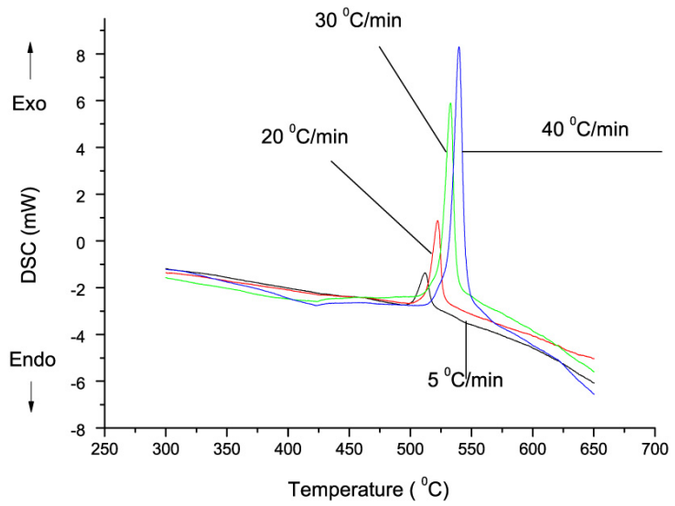

Fig. 14. DSC curves at different heating rates

The different algebraic expressions of conversion functions for solid state transformations are given in Table 3.

Fig. 14 shows the continuous DSC curves of $Fe_{81}B_{13}Si_4C_2$ ribbon in temperature range 300-650^{o}C taken at four different heating rates. All curves contain a single well formed exothermic peak representing crystallization in the temperature range 500-560^{o}C.

Mechanism label	$f(\alpha)$	$g(\alpha)$
Power law P4	$4\alpha^{3/4}$	$\alpha^{1/4}$
Power law P3	$3\alpha^{2/3}$	$\alpha^{1/3}$
Power law P2	$2\alpha^{1/2}$	$\alpha^{1/2}$
Power law P3/2	$3/2\alpha^{1/3}$	$\alpha^{2/3}$
Avrami-Erofeev A3/2	$3/2(1-\alpha)[-\ln(1-\alpha)]^{1/3}$	$[-\ln(1-\alpha)]^{2/3}$
Avrami-Erofeev A2	$2(1-\alpha)[-\ln(1-\alpha)]^{1/2}$	$[-\ln(1-\alpha)]^{1/2}$
Avrami-Erofeev A3	$3(1-\alpha)[-\ln(1-\alpha)]^{3/2}$	$[-\ln(1-\alpha)]^{1/3}$
Avrami-Erofeev A4	$4(1-\alpha)[-\ln(1-\alpha)]^{3/4}$	$[-\ln(1-\alpha)]^{1/4}$
Prout-Tompkins B1	$\alpha(1-\alpha)$	$\ln[\alpha(1-\alpha)^{-1}]$
Šesták-Berggren	$\alpha^{N}(1-\alpha)^{M}$	-
One dimensional phase boundary R1	1	α
Contracting cylinder R2	$2(1-\alpha)^{1/2}$	$1-(1-\alpha)^{1/2}$
Contracting sphere R3	$3(1-\alpha)^{2/3}$	$1-(1-\alpha)^{1/3}$
D1 One-dimensional diffusion	$1/2\alpha$	α^2
D2 Two-dimensional diffusion	$[-\ln(1-\alpha)]^{-1}$	$(1-\alpha)\ln(1-\alpha)+\alpha$
D3 three-dimensional diffusion	$3/2(1-\alpha)^{2/3}[1-(1-\alpha)^{1/3}]^{-1}$	$[1-(1-\alpha)^{1/3}]^2$
D4 Ginstling-Brounshtein	$3/2[(1-\alpha)^{-1/3}-1]^{-1}$	$(1-2\alpha/3)-(1-\alpha)^{2/3}$
F1 First-order	$1-\alpha$	$-\ln(1-\alpha)$
F2 Second-order	$(1-\alpha)^2$	$(1-\alpha)^{-1}$
F3 Third-order	$1/2(1-\alpha)^3$	$(1-\alpha)^{-2}$

Table 3. Algebraic expressions of conversion functions for solid state transformations

All values of initial (T_i), maximal (T_p) and final temperature (T_f) for both exo-peaks are shifted to higher values with increasing heating rate indicating the presence of kinetic effects (Table 4). The shape of DSC curves depends on the heating rate, because, as the values of shape factor S show, asymmetry of peaks increases with the decrease of heating rates indicating that the heating rate has a strong influence on the crystallization process. The values of shape factor S is obtained as the ratio of half-widths (left and right) for individual crystallization peaks for particular heating rate. The fractional extent of the sample transformed into crystalline phase, α, has been obtained from the DSC curve as a function of temperature (T) (Minić & Adnađević, 2008). At any temperature T, α is defined as $\alpha = S_T/S$, where S is the total area of the exotherm, between the temperature T_i, of the onset of crystallization and the temperature T_f, of the end of crystallization, and S_T is the area between the initial temperature T_i and a generic temperature, T, ranging between T_i and T_f (Friedman, 1964). The plots of α versus T at different heating rates for the considered crystallization process are shown in Fig. 15.

The sigmoid shape of fractional conversion curves in Fig. 15 indicates, for all heating rates, a slow initial period corresponding to nucleation with increasing rate caused by the increase

of specific surface area of nuclei. The saturation part that follows is the consequence of nuclei merging together causing a decrease in their surface area.

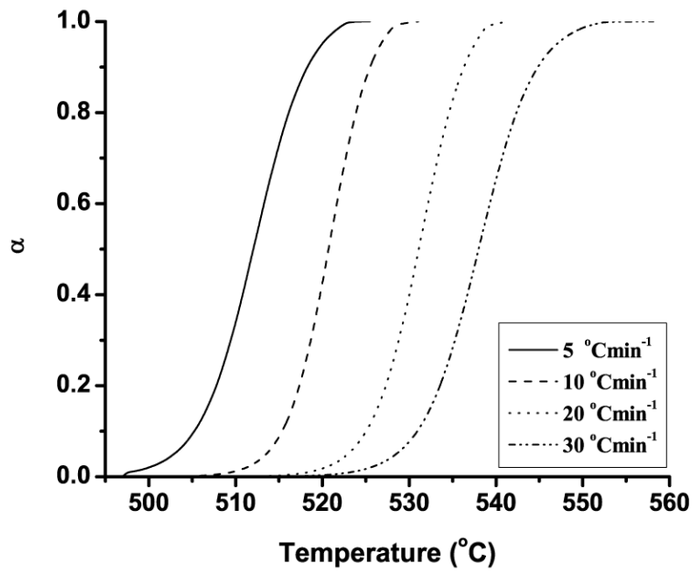

Fig. 15. Fractional conversion (α) as a function of temperature (*T*) for the crystallization alloy at different heating rates (5, 10, 20 and 30°Cmin^{-1}).

2.7.1 The overall apparent activation energy of crystallization

The overall activation energy of crystallization of an amorphous alloy under linear heating condition can be determined by the Kissinger as well as by the Ozawa peak method relating to the dependence of exothermic peak temperature *Tp* on heating rate β.

Kissinger (Kissinger, 1957) proposed that the activation energy can be determined according the equation

$$\ln\left(\frac{\beta}{T_p^2}\right) = \ln\left(\frac{AR}{E_a}\right) - \frac{E_a}{RT} \tag{6}$$

For the determination the activation energy in non-isothermal conditions Ozawa (Ozawa, 1970) proposed the equation:

$$\ln\beta = \ln\frac{AE_a}{R}C - 1.0516\frac{E_a}{RT_p} \tag{7}$$

The values of peak temperatures together with values of kinetic parameters (E_a and ln*A*) calculated by both methods and the symmetry factors (SF) are given in the Table 4.

β ^{o}Cmin^{-1}	T_i ^{o}C	T_p ^{o}C	T_f ^{o}C	S	Ozawa		Kissinger	
					E_a kJmol^{-1}	A × 10^{22} min^{-1}	E_a kJmol^{-1}	A × 10^{21} min^{-1}
5	492	512	542	0.59	338.0 +1.8	1.10 ± 2.3	351.2±1.8	3.06 ±2.3
10	501	520	546	0.59				
20	509	531	554	0.70				
30	513	538	560	0.75				

Table 4. Values of T_i, T_p, T_f and S for crystallization of the amorphous $Fe_{81}B_{13}Si_4C_2$ alloy upon continuous heating at different heating rates.

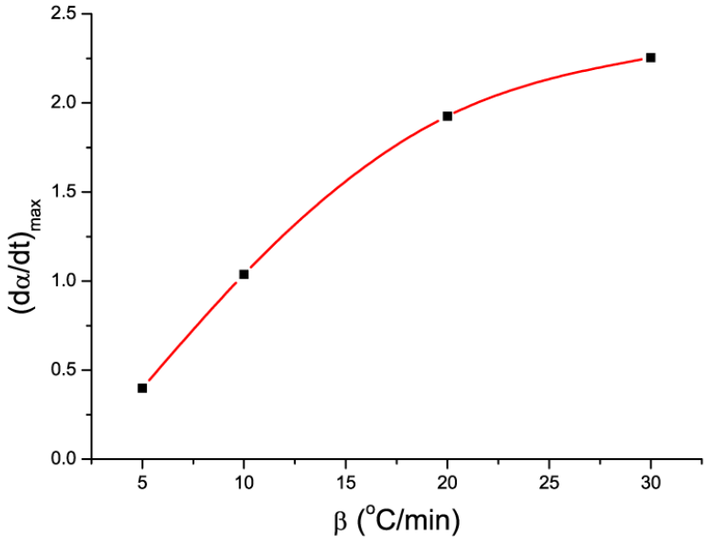

Fig. 16. The dependence of maximum rate of crystallization on heating rate.

The dependence of maximum of rate on rate of heating (Fig. 16) shows the growth of maximum of rate of crystallization with respect to the rate of heating. It indicates that the rate of crystallization reaches a saturation point at high heating rates.

The activation energy of crystallization process involving formation of nuclei and their growth, according to some opinions, has no physical meaning, just empirical significance and only establishes the dependence of the rate of conversion on temperature. This energy can be spent, not just for overcoming the activation barrier but also for its downturn due to cooperative displacement of groups of atoms. Finally, the crystallization of amorphous alloys is a very complicated process accompanied by nucleation and growth of various crystal phases under continuously varied conditions in the conversion zone. With the multitude of possible ways of conversions, only those mechanisms and activated complexes of the crystallization process will be realized that have the highest probability at a given temperature. Any change in crystallization conditions, such as heating rate, can result in change of the mechanism and main activation complex of the crystallization process. Thus, high values of activation energy of crystallization of amorphous alloys, first of all, indicate that a large number of atoms participate in an elementary act of structure reorganization, as well as high complexity of the transformation processes.

2.7.2 The dependence of apparent activation energy on range of conversion

On the basis of dynamic DSC measurements for different heating rates, isoconversional method of Kissinger-Akahira-Sunose method, also known as the „model-free method", enables the determination values of E_a over a wide range of α without the determination of the conversion function (Kissinger, 1957; Akahira, Sunose, 1971). This model involves measuring the temperatures T_a corresponding to fixed values of the crystallized volume fraction, a, for different heating rates, β, and application of the relation:

$$\ln\left(\frac{\beta_i}{T_{\alpha,i}^2}\right) = \ln\left(\frac{AR}{E_{a,\alpha}}F(\alpha)\right) - \frac{E_{a,\alpha}}{RT_{\alpha.i}} \tag{8}$$

where a subscript α designates values related to a given conversion degree, and i is a number of the non-isothermal experiment conducted at the heating rate β_i.

The left-hand side of Eq. (8) is linear with respect to the inverse temperature, $1/T_a$, and enables the activation energy to be evaluated using a linear regression method. In case of a single step process, a constant value of $E_{a(a)}$ is obtained. On the other hand, the dependence of $E_{a(a)}$ on α indicates complex process involving more than one step with different activation energies. It can be observed that the apparent activation energy for the considered crystallization process (Fig. 17) is practically constant in the $0.05 \leq \alpha \leq 0.7$ range indicating the existence of a single-step reaction. (Vyazovkin, 2000; Opfermann & Flammersheim, 2003). The average value of apparent activation energy was determined as E_a = 356.5 ± 5.5 kJmol^{-1}.

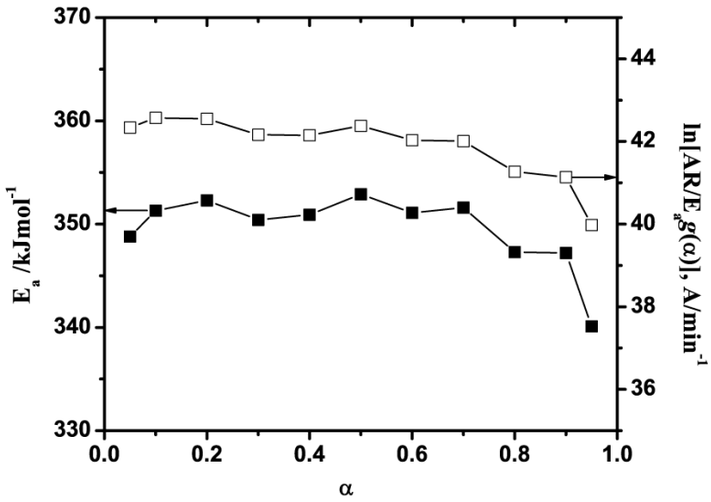

Fig. 17. Apparent activation energies (E_a) and the intercepts as function of the crystallized fraction α.

2.7.3 Preliminary determination of kinetic model

For the preliminary determination of kinetic model of the crystallization process, Dollimore's method was used (D. Dollimore, 1991, 1992; Lee, 1998).

β (°C/min)	α_{max}	$\frac{\Delta LoT}{\Delta HiT}$	Half-width (°C)	T_i	T_f
5	0.51	1.0	9.5	sharp	sharp
10	0.53	1.0	9.5	sharp	sharp
20	0.53	0.9	10.0	sharp	sharp
30	0.55	0.8	11.0	sharp	sharp

Table 5. Parameters describing the asymmetric DSC peaks of crystallization α-Fe phase in amorphous $Fe_{81}B_{13}Si_4C_2$ alloy

This model is based on the "sharpness" of initial and final temperature of differential rate curves, Fig. 18, as well as on its asymmetry. The "sharpness" of the initial and final temperatures is influenced by kinetic factors, and especially by the mechanism of the process. Certain kinetic models lead to an asymptotic or diffuse departure from the base line in the differential form of the thermal curve, while others produce a very sharp approach to the final plateau. The investigation of these parameters that describe geometry and asymmetry of the differential rate curves can be an indicator of the probable kinetic mechanism. According to these parameters, different types of kinetic mechanisms have been listed (Lee, 1998). So, when the crystallization process is not complex the qualitative approach to its kinetics may be obtained using parameters such as α_{max} or $(d\alpha/dt)_{max}$, the shape of the initial and final temperatures as well as peak temperature (T_p) or half-width from differential rate curves.

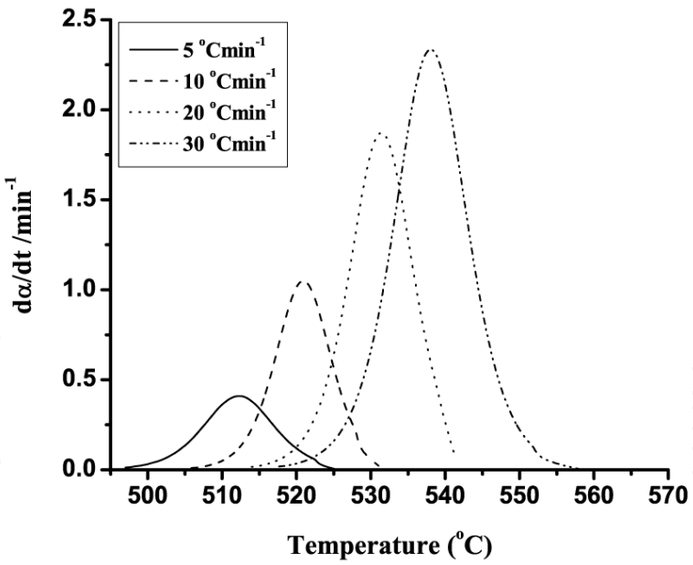

Fig. 18. Differential rate curves ($d\alpha/dt$ vs. T) for different heating rates (β = 5, 10, 20 and 30°Cmin^{-1}).

In this case, Dollimore's procedure was applied to the conversion and differential rate curves (Fig.18) whose slight asymmetry is observed between T_i and T_f. The other parameters such as the conversion at the rate of maximum crystallization, α_{max}, peak temperature, T_p, at $(d\alpha/dt)_{max}$, and the ratio ΔLoT/ΔHiT (shape factor), which is the ratio between the low and high temperature points at half-width of the differential rate curve peak are presented in

Table 5. It is clearly seen that the position of the broadening exotherm, which is connected with the crystallization, was shifted toward higher temperature with the increase of the heating rate as well as asymmetry of peaks. This suggests that the crystallization process should not be characterized by a definite critical temperature independent of the heating rate. The determined values of α_{max} for different heating rates were in the range from 0.51 to 0.55. These results indicate that the non-isothermal crystallization mechanism of α-Fe in amorphous $Fe_{81}B_{13}Si_4C_2$ alloy can not be fully described within the JMA (Johnson-Mehl-Avrami) models (A2, A3 and A4, Group A).

2.7.4 Determination of the kinetic model

General equation, enabling the analysis of conversion kinetics involving nucleation and growth in solid phase was proposed by Avrami (Avrami, 1939):

$$\alpha(t) = 1 - \exp[-(kt)^n], \tag{9}$$

where $\alpha(t)$ is conversion degree, n is kinetic exponent, $k=k_o\exp(-E_a/RT)$.

Differentiation of this equation with respect to time gives the rate equation, known as the JMA equation:

$$\left(\frac{\mathrm{d}\alpha}{\mathrm{d}t}\right) = kn(1-\alpha)[-\ln(1-\alpha)]^{1-1/n}. \tag{10}$$

The JMA equation is based on assumptions of isothermal crystallization, homogenous or heterogeneous nucleation at randomly dispersed particles of the second phase. The growth rate of new phase is independent of time and controlled by temperature and low anisotropy of growing crystals. However if the entire nucleation process takes place during the early stage of transformation and becomes negligible afterwards, JMA equation can also be applied to non-isothermal conditions (Henderson, 1979).

The validity of listed assumptions is not given a priori and simple and reliable testing methods were developed (Málek, 1992, 1995; Gotor et al, 2000; Criado et al, 2003). Once the apparent activation energy has been determined, it is possible to find the kinetic model which best describes the measured set of thermoanalytical data. It can be shown that, for this purpose, it is useful to define two special functions y(α) and z(α), which can easily be obtained by simple transformation of the experimental data. The conversions, in which the y(α) and z(α) functions exhibit the maximum values are designated as α_y^* and α_z^*, respectively. Under non-isothermal conditions these functions can be expressed as follows (Málek, 1992, 1995, 2000):

$$y(\alpha) = \left(\frac{d\alpha}{dt}\right)\exp\left(\frac{E_a}{RT}\right) = Af(\alpha) \tag{11}$$

$$z(\alpha) \approx \left(\frac{d\alpha}{dt}\right)T^2 \tag{12}$$

The maximum of the y(α) function for the JMA model depends on the value of the kinetic exponent:

$$\alpha_y^* = 0 \quad \text{for } n \leq 1$$

$$\alpha_y^* = 1\text{-}\exp(n^{-1}\text{-}1) \quad \text{for } n > 1$$

The value of α_y^* is always lower than the maximum of value for α_z^*. For JMA model, α_z^* =0.632. This value is characteristic "fingerprint" of the JMA model and it can be used as a simple test of the applicability of this model.

The obtained normalized functions y(α) and z(α), Fig 19, are independent on the heating rate (β) of the system, and the both functions exhibits the well-defined maxima which were located at exactly defined value of α (α_y^* for the y(α) function and α_z^* for z(α) function, respectively), Table 6.

β ^{o}C min^{-1}	α_y^*	α_z^*
5	0.41 ± 0.01	0.53 ± 0.01
10	0.42 ± 0.01	0.51 ± 0.01
20	0.42 ± 0.01	0.55 ± 0.03
30	0.41 ± 0.01	0.52 ± 0.01

Table 6. The maximum of α_y and α_z for the different heating rates

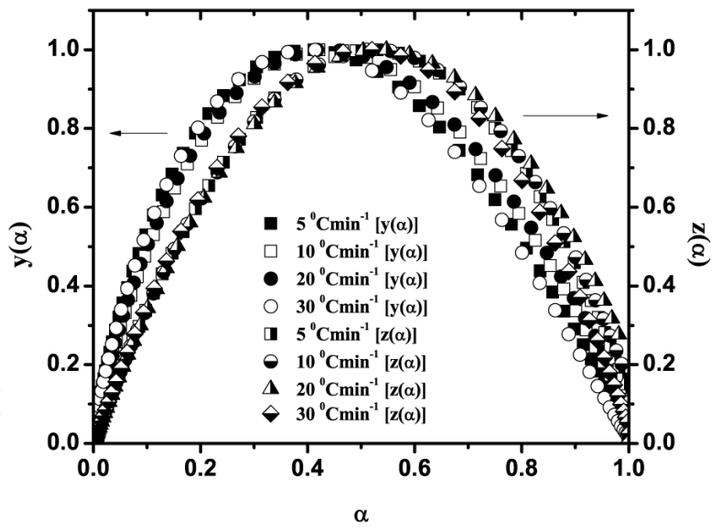

Fig. 19. Normalized $y(a)$ and $z(a)$ functions at the different heating rates.

From Table 6, it can be seen that the values of α_y^* fall into the range $\alpha_y^* \in (0, \alpha_z)$ ($0.41 \leq \alpha_y^* \leq 0.42$) and the values of α_z^* are less than 0.632 ($0.51 \leq \alpha_z^* \leq 0.55$). From the obtained results, it follows that the conditions of validity of the JMA model are not fulfilled for crystallization of *a*-Fe. The displacement of α_z^* in lower value range indicates complexity of the process and can be caused by the influence of surface nucleation or the effect of released crystallization heat on temperature distribution within the sample. However, the relatively high value of α_y^* indicates an increasing effect of the crystallized phase to overall

crystallization kinetics, where the crystallized phase further increases the rate of the crystallization. Such autocatalytic behavior can be well described using an empirical two parameter Šesták-Berggren's kinetic model (Šesták, Berggren, 1971; Málek, et al. 1989). This model is based on the equation:

$$f(\alpha) = \alpha^M (1-\alpha)^N , \tag{13}$$

where M and N represents the kinetic exponents.

In this case the expression for reaction rate of the investigated crystallization process can be given as:

$$\frac{d\alpha}{dt} = A \exp\left(-\frac{E_a}{RT}\right) \alpha^M (1-\alpha)^N \tag{14}$$

For this model, the ratio of the kinetic exponents $p = M / N$ can be calculated from the maximum of the y (α) function (Málek, 2000):

$$p = \frac{M}{N} = \frac{\alpha_y^*}{\left(1-\alpha_y^*\right)} . \tag{15}$$

Introducing this equation in equation this (13) gives:

$$\ln\left[\left(\frac{d\alpha}{dt}\right)\exp\left(\frac{E_a}{RT}\right)\right] = \ln A + N \ln\left[\alpha^p (1-\alpha)\right]. \tag{16}$$

This equation describes the processes of nucleation and growth in non-crystalline solids very well. The parameters M and N define relative contributions of acceleratory and decay regions of the kinetic process. From the linear dependence $\ln\left[(d\alpha / dt)\exp(E_a / RT)\right]$ =f($\ln\left[\alpha^p(1-\alpha)\right]$), it is possible to obtain the kinetic exponent N and the pre-exponential factor, ln A. The value of kinetic exponent M can be obtained directly from eq. (15).

β °C/min	M	N	ln$A$ (*10^{22})
5	0.75 ± 0.03	1.08 ± 0.10	9.0±0.2
10	0.66 ± 0.05	0.92 ± 0.05	10.7±0.3
20	0.64 ± 0.05	0.89 ± 0.07	9.4±0.2
30	0.81 ± 0.10	1.17 ± 0.04	10.6±0.2
Average	0.72 ± 0.06	1.02 ± 0.07	9.9±0.2

Table 7. Kinetic exponents M and N at different heating rates (Adnađević et al., 2010)

Table 7 lists the values of kinetic exponents M and N, as well as the values of ln$A$ obtained by the procedure described above, for the considered crystallization process at different heating rates.

The obtained values of kinetic exponents M and N vary a little with respect to heating rate β. The values of M vary in the range of $0.64 \le M \le 0.81$ with average value of $M_{av} = 0.72$. The values of N vary in the range of $0.89 \le N \le 1.17$ with average value of $N_{av} = 1.02$. The values of the pre-exponential factor ($\ln A$) are independent on the heating rate (β), within the limits of the experimental error. It was shown that this two parameter autocatalytic model has physical meaning only for M<1(Gotor, et al. 2000).

In order to check the established kinetic model we applied the "Master-plot" method (Criado, et. al 2003; Gotor, 2000). Using the value at α = 0.5 as a reference point, the following differential master equation is easily derived from eq. (4):

$$\frac{f(\alpha)}{f(0.5)} = \frac{d\alpha / dt}{(d\alpha / dt)_{0.5}} \frac{\exp(E_a / RT)}{\exp(E_a / RT_{0.5})} \tag{17}$$

where $(d\alpha/dt)_{0.5}$, $T_{0.5}$ and f (0.5) are the reaction rate, the temperature reaction and the differential conversion function, respectively at $a = 0.5$.

The left side of Eq. (17) is a reduced theoretical curve which is characteristic of each kinetic function. The right side of the equation is associated with the reduced rate and can be obtained from experimental data if the apparent activation energy is known and remains constant throughout the reaction. Comparison of both sides of Eq. (17) tells us which kinetic model describes an experimental reaction process. It can be seen in Fig. 20, using the average value for the apparent activation energy determined from Kissinger-Akahira-Sunose isoconversional method, the suggested kinetic model works very well in the entire conversion range. Therefore, the Šesták-Berggren autocatalytic model represents the best reaction model for describing the crystallization process of α-Fe in the amorphous $Fe_{81}B_{13}Si_4C_2$ alloy. The higher value of N exponent designates that the formed crystallized phase has the decisive influence on the kinetics of transformation and the rate of growth. In the propagation process, on account of overlapping of nuclei during growth, it acts to retard crystallization rate. Bearing this in mind, we can suppose that in the amorphous alloy, the α-Fe embryos

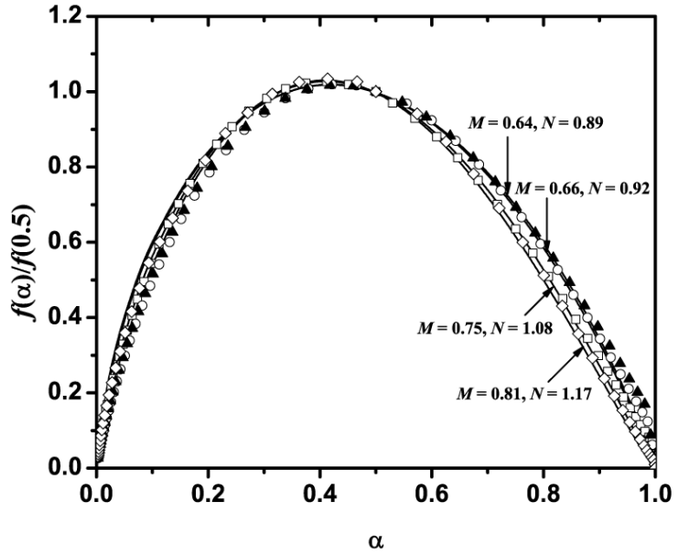

Fig. 20. The theoretical (solid line) and experimental differential master plots of $f(\alpha)/f(0.5)$ versus α for different heating rates: (□) 5 °Cmin^{-1}; (○) 10 °Cmin^{-1}; (▲) 20 °Cmin^{-1} and (◊) 30 °Cmin^{-1}.

already exist at $T \leq 500^{o}C$ and at $T \geq 500^{o}C$ these embryos are momentarily transformed into nuclei. The established acceleration of crystallization process is a consequence of significant increase of strain in alloy, which arises on account of formation of α-Fe.

2.7.5 Morphology of crystal growth

For non-isothermal crystallization, where the volume fraction of crystalline phase α precipitated in glass heated at a uniform heating rate β is related with the activation energy E_a, Matusita et al. proposed the following relation (Matusita & S. Sakka, 1979, 1980; Matusita, et al. 1984):

$$\ln[-\ln(1-\alpha)] = -n\ln\beta - \frac{1.052mE_a}{RT} + const\,, \tag{18}$$

where m and n are constants with values between one and four depending on the morphology and kinetics of the growth nuclei, Table 8.

Mechanism	n	m
Bulk nucleation		
Three dimensional growth	4	3
Two dimensional growth	3	2
One dimensional growth	2	1
Surface nucleation	1	1

Table 8. Values of constants n and m for different crystallization mechanisms

The values of n obtained from the slopes of linear plots ln[-ln (1-α)] versus $-\ln\beta$ at different temperatures for considered crystallization process are given in Table 9. For all considered temperatures, the value of n is ≈ 4.0, within the limits of experimental errors. It follows, then, that the kinetics of crystallization process is independent from the temperature.

The crystallization exponent n is connected with the number of growth dimensions (m) and the number of nuclei forming stages (s) (Matusita, Sakka, 1979) by the following equation

$$n = m + s \tag{19}$$

where m is the number of growth dimensions as defined in Table 8, s is the number of the nuclei forming stages (s = 0 – at instantaneously nucleation; s = 1 – at constant nucleation rate and s > 1 at self-acceleratory nucleation rate).

In order to describe the crystallization process in detail, the value of parameter m should be determined from the plot of ln [-ln (1-α)], because a function of reciprocal temperature is linear with a slope of $1.051\times(m+1)E_a/R$, using the value of activation energy determined above.

Temperature ^{o}C	n	β $^{o}C/min$	m	s
518	3.92	5	2.84	1.16
520	4.08	10	3.08	0.92
522	4.07	20	3.22	0.78
		30	2.84	1.16

Table 9. The values of n at three temperatures and values of m and s for four different heating rates

The values of parameters *m* and *s* obtained at the different heating rates for the investigated crystallization process of α-Fe in $Fe_{81}B_{13}Si_4C_2$ amorphous alloy are given in Table 9. Based on the obtained values of parameters *m* and *s*, at the different heating rates, (Table 9), we asserted with high degree of reliability, that the nucleation process of α-Fe occurs within amorphous alloy with a constant rate, in three effective directions (three-dimensional growth) proceeding with constant nucleation rate.

3. Conclusion

Metallic amorphous alloy are a class of materials which has seen dramatic developments in recent times with design of materials stable enough to allow bulk production. While the functional properties of amorphous alloys allow for many possible fields of application, they can also be used as precursors in preparation of nanocomposite materials composed of nanocrystals in the amorphous matrix. These nanocomposites often exhibit superior mechanical, electrical and magnetic properties to both purely amorphous and purely crystalline materials. Thermal treatment of amorphous alloys can allow for controlled crystallization, leading to formation of nanocomposite materials with targeted properties.

$Fe_{81}B_{13}Si_4C_2$ alloy undergoes multi-step crystallization process as a result of thermal treatment. The changes in microstructure cause changes in electrical, magnetic and mechanical properties of the alloy as the alloy structure changes from predominantly amorphous to crystal/amorphous nanocomposite to nanocrystalline composite of α-Fe and Fe_2B phases.

4. References

Adnađević, B.; Janković B. & Minić D. M.; (2010), Kinetics of the apparent isothermal and non-isothermal crystallization of the α-Fe phase within the amorphous $Fe_{81}B_{13}Si_4C_2$ alloy, Journal of Physical Chemistry of Solids, vol. 71, pp. 927-934

Akahira, T. & Sunose, T. (1971) Trans. Joint Convention of Four Electrical Institutes, paper no. 246 (1969), Research Report, Chiba Institute of Technology, vol. 16, pp. 22-31

Avrami, M. (1939), Kinetics of Phase Change. I General Theory, Journal of Chemical Physics, vol. 7, No. 12, pp. 1103-1113

Blagojević, V. A.; Minić, D. M.; Žak, T.; Minić, D. M. (2011), Influence of thermal treatment on structure and microhardness of $Fe_{75}Ni_2Si_8B_{13}C_2$ amorphous alloy, Intermetallics vol. 19, pp. 1780-1785

Balberg, I. & Helman, J. S. (1978), Critical behavior of the resistivity in magnetic systems. II. Below Tc and in the presence of a magnetic field, Physical Review B, vol. 18, No. 1, pp. 303-318

Böhnke, G.; Kaul, S. N.; Kettler, W. & Rosenberg, M. (1983), Critical behaviour of the electrical resistivity in amorphous ferromagnetic alloys, Solid State Communications, vol. 48, No. 9, pp. 743-746

Criado, J. M.; Pérez-Maqueda, L. A.; Gotor, F. J.; Málek, J. & Koga, N. (2003), A unified theory for the kinetic analysis of solid state reactions under any thermal pathway, Journal of Thermal Analysis and Calorimetry, vol. 72, No. 3, pp. 901-906

Dollimore, D.; Evans, T.A.; Lee, Y.F. & Wilburn, F.W. (1991), Calculation of activation energy and pre-exponential factors from rising temperature data and the generation of TG and DTG curves from A and E values, Thermochimica Acta, vol. 188, No. 1, pp. 77-85

Dollimore, D.; Evans, T.A.; Lee, Y.F.; Pee, G.P. & Wilburn, F.W. (1992), The significance of the onset and final temperatures in the kinetic analysis of TG curves, Thermochimica Acta, vol. 196, No. 2, pp. 255-265

Friedman, H. L. (1964), Kinetics of thermal degradation of char-forming plastics from thermogravimetry. Application to a phenolic plastic, Journal of Polymer Science Part C: Polymer Symposia, vol. 6, No. 1, pp. 183-195

Gotor, F. J.; Criado, J. M.; Málek, J. & Koga, N. (2000), Kinetic Analysis of Solid-State Reactions: The Universality of Master Plots for Analyzing Isothermal and Nonisothermal Experiments, Journal of Physical Chemistry A, vol. 104, No. 46, pp. 10777-10782

Henderson, D. W. (1979), Experimental analysis of non-isothermal transformations involving nucleation and growth, Journal of Thermal Analysis and Calorimetry, vol. 15, No. 2, pp. 325-331

Kissinger, H. E. (1957), Reaction Kinetics in Differential Thermal Analysis, Analytical Chemistry, vol. 29, No. 11, pp. 1702-1706

Klement, W.; Willens, R. H & Duwez, P.O.L. (1960), Non-crystalline Structure in Solidified Gold-Silicon Alloys, Nature, vol. 187, No. 4740, pp. 869–870

Lass, E. A.; Zhu, A.; Shiflet, G. J. & Poon, S. J. (2010), A short-range ordering description of amorphous metal alloys using the central atoms model, Acta Materialia, vol. 58, No. 16 pp. 5460-5470

Lee, Y.F. & Dollimore, D. (1998), The identification of the reaction mechanism in rising temperature kinetic studies based on the shape of the DTG curve, Thermochimica Acta, vol. 323, No. 1-2, pp. 75-81

Libermann H. & Graham C. (1976), Production Of Amorphous Alloy Ribbons And Effects Of Apparatus Parameters On Ribbon Dimensions, IEEE Transactions on Magnetics, vol. 12, No. 6, pp. 921

Málek, J.; Criado, J. M.; Šesták, J. & Militky, J. (1989), The boundary conditions for kinetic models, Thermochimica Acta, vol. 153, pp. 429-432

Málek, J. (1992), The kinetic analysis of non-isothermal data, Thermochimica Acta, vol. 200, pp. 257-269

Málek, J. (1995), The applicability of Johnson-Mehl-Avrami model in the thermal analysis of the crystallization kinetics of glasses, Thermochimica Acta, vol. 267, pp. 61-73

Málek, J. (2000), Kinetic analysis of crystallization processes in amorphous materials, Thermochimica Acta, vol. 355, No. 1-2, pp. 239-253

Maričić, A.; Minić, D. M.; Blagojević, V. A.; Kalezić-Glišović, A.; Minić, D. M. (2012), *Effects of structural relaxation on functional properties of amorphous alloy* $Fe_{73.5}Cu_1Nb_3Si_{15.5}B_7$, Intermetallics vol. 21, pp. 45-49

Matusita, K. & Sakka, S. (1979), Kinetic study of the crystallisation of glass by differential scanning calorimetry, Physics and Chemistry of Glasses, vol. 20, pp. 81-85

Matusita, K. & Sakka, S. (1980), Kinetic study of crystallization of glass by differential thermal analysis—criterion on application of Kissinger plot, Journal of Non-Crystalline Solids, vol. 38-39, No. 2, pp. 741-746

Matusita, K.; Konatsu, T. & Yokota, R. (1984), Kinetics of non-isothermal crystallization process and activation energy for crystal growth in amorphous materials, Journal of Materials Science, vol. 19, No. 1, pp. 291-296

Minić, D. M.; Maričić, A., Dimitrijevic, R. Z.; Ristić, M. M. (2007), Journal of Alloys and Compdounds, vol. 430, pp. 241-245

Minić, D. M.; & Adnađević, B. (2008), Mechanism and kinetics of crystallization of α-Fe in amorphous $Fe_{81}B_{13}Si_4C_2$ alloy, Thermochimica Acta, vol. 474, No. 1-2, pp. 41-46

Minić, D. M.; Maričić, A. & Adnađjević, B. (2009), Crystallization of α-Fe phase in amorphous $Fe_{81}B_{13}Si_4C_2$ alloy, Journal of Alloys and Compounds, vol. 473, pp. 363-367

Minić, D. M.; Minić, D. G. & Maričić, A. (2009), Stability and crystallization of $Fe_{81}B_{13}Si_4C_2$ amorphous alloy, Journal of Non-Crystalline Solids, vol. 355, No. 50-51, pp. 2503-2507

Minić, D. M.; Plazinić, M. ; Živanić, J. & Maričić, A. (2010), Influence of Structural Transformations on Electric and Magnetic Properties of $Fe_{81}B_{13}Si_4C_2$ Amorphous Alloy, Science of Sintering, vol. 42, pp. 61-68

Minić, D. M.; Blagojević, V.; Minić, D. G.; Gavrilović, A.; Rafailović, L. (2011), Influence of thermally induced structural transformations on hardness in $Fe_{89.8}Ni_{1.5}Si_{5.2}B_3C_{0.5}$ amorphous alloy, Journal of Alloys and Compounds vol. 509, pp. 8350-8355

Minić, D. M.; Minić, D. M.; Žák, T.; Roupcova, P. & David, B. (2011), Structural transformations of $Fe_{81}B_{13}Si_4C_2$ amorphous alloy induced by heating, Journal of Magnetism and Magnetic Materials, vol. 323, No. 5, pp. 400-404

Minić, D. M.; Blagojević, V. A.; Minić, D. M.; Gavrilović, A. & Žak, T. (2011), Influence of microstructure on microhardness of $Fe_{81}Si_4B_{13}C_2$ amorphous alloy after thermal treatment, Metallurgical and Materials Transactions A, vol 42, pp. 4106-4112

Minić D. M; Blagojević V. A; Minić D. M.; Žák T(2011), Influence of microstructural inhomogeneouity of individual sides of $Fe_{81}Si_4B_{13}C_2$ amorphous alloy ribbon on thermally induced structural transformations, Materials Chemistry and Physics, vol. 130, pp. 980-985

Opfermann, J. & Flammersheim, H. J. (2003), Some comments to the paper of J.D. Sewry and M.E. Brown: "Model-free" kinetic analysis, Thermochimica Acta, vol. 397, No. 1-2, pp. 1-3

Ozawa, T. (1970), Kinetic analysis of derivative curves in thermal analysis, Journal of Thermal Analysis and Calorimetry, vol. 2, No. 3, pp. 301-324

Ponnambalam, V.; Poon, S. J. & Shiflet, G. J. (2004), Fe-based bulk metallic glasses with diameter thickness larger than one centimeter, Journal of Materials Research vol. 19, No. 5, pp. 1320-1323

Ribić-Zelenović, L.; Rafailović, L.; Spasojević, M. & Maričić, A. (2008), Correlation between electron state density change and the electrical resistivity and magnetic permeability changes in the nanostructured powder of the NiMo alloy, Physica B: Condensed Matter, vol. 403, No. 12, pp. 2148-2154

Saegusa, N. & Morrish, A. H. (1982), Atomic rearrangements and crystalline transformations in amorphous Fe81B13.5Si3.5C2, Physical Review B, vol. 26, No. 1, pp. 305-314

Šesták, J. & Berggren, G. (1971), Study of the kinetics of the mechanism of solid-state reactions at increasing temperatures, Thermochimica Acta, vol. 3, No. 1, pp. 1-12

Vyazovkin, S. (2000), Computational aspects of kinetic analysis.: Part C. The ICTAC Kinetics Project — the light at the end of the tunnel?, Thermochimica Acta, vol. 355, No. 1-2, pp. 155-163

Williamson, G. K. & Hall, W. (1953), X-ray line broadening from filed aluminium and wolfram, Acta Metallurgica, vol. 1, No. 1, pp. 22-31

Žák, T. (1999) In: Mössbauer spectroscopy in Material Science, Eds. M. Miglierini and D. Petridis, NATO Science Series, Kluwer, Dordrecht, 1999, pp. 385

Žák, T. & Jirásková, Y. (2006), CONFIT: Mössbauer spectra fitting program, Surface Interface Analysis, vol. 38, No. 4, pp. 710-714

IntechOpen